A capacitive-inductive dual modality imaging system for non-destructive evaluation applications

Abstract

A dual modality imaging system is proposed which can automatically switch between capacitive imaging and inductive imaging modes. After a single scan over the specimen under test, two types of image, namely capacitive and inductive, can be obtained by the proposed system. For an insulated metallic structure, the capacitive image contains the defect information in the insulation layer and on the top surface of the conducting layer, while the inductive image contains the defect information within the conducting region. A theoretical explanation of the imaging mechanisms for the capacitive and inductive modes are given. The results of finite element modelling show the perturbation of the probing fields due to defects in the two imaging modes. Experimental results from a dual modality imaging system are also presented, demonstrating detection of defects in insulator-metal hybrid structures to verify the effectiveness of this approach.

Keyword: Non-destructive Evaluation, defect detection, dual modality imaging

1. Introduction

Electromagnetic nondestructive tests are important and widely used within the field of nondestructive evaluation (NDE). The selection of measurement method is determined by the permittivity, conductivity and permeability of the material of interest. Generally, capacitive measurements are suitable for evaluating dielectric materials or materials with very low conductivity; For example, capacitive sensors have been used to inspect composite structures [1-5], concrete [6, 7] and wire insulation [8]. Magnetic induction methods such as Alternating Current Field Measurement (ACFM) and eddy current techniques are suitable for conducting materials. Thus, for example, ACFM has been used to detect and characterize cracks in tubes and pipe strings [9, 10]. Eddy current techniques can detect surface and near surface cracks [11] and cracks near faster holes [12], and also to measure metal thickness [13], quantify pocket length of an angled crack [14], and detect fibre waviness in carbon fibre composite [15].

In a typical case, insulators and conductors have to be inspected with different techniques and/or systems. However, some specific applications require simultaneous inspections of both kinds of materials. For example, for the insulated pipes extensively used in the petroleum and petrochemical industries, Corrosion Under Insulation (CUI) is a major concern. CUI is difficult to find because the insulation covers the corrosion problem until it is too late. Removing insulation, inspecting, and then reinstating the insulation after inspection is an expensive process. Inspecting without removing insulation greatly reduces the cost of inspections. Current research focuses on penetrating through the thick insulation and inspect the metal surface [16, 17]. However, in practice, it is also useful to find the defects and water intrusion in the insulation layer as causes of CUI, before the actual occurence of CUI. An inspection system with sensitivities to defects in both insulation layer and on the pipe surface, preferably with the ability to discriminate the defect location, is thus needed.

Attempts at combining capacitive and inductive measurements have been reported in previous work. Inductive-capacitive dual modality sensors have been developed to detect and distinguish between conductive and dielectric materials, by switching modes of operation for a physical combination of two sensors [18], or by identifying the predominant sensor response above and below the resonant frequency of a combined capacitive-inductive sensor [19]. The capacitive coupling effects of eddy current probes at high operating frequency can also be used to detect defects in non-conducting specimens [20]. An electromagnetic sensor with a novel measurement strategy, which can operate simultaneously in capacitive and inductive modalities with sensitivities to permittivity, conductivity, and permeability, has also been reported [21]. These studies were mainly focused on crack/flaw detection or parameter estimation directly from measurements. However, to provide a visual interpretation of the possible defects, an imaging system with a dual modality sensor is required.

This paper proposes a novel imaging system with a coplanar capacitive-inductive dual modality imaging sensor. The coplanar sensor has several advantages, which include high sensitivity due to small lift-off effects, flexible attachment to a complex surface

and ease of manufacture. The dual modality sensor is sensitive to both permittivity variations in the capacitive imaging mode, and conductivity variations in the inductive imaging mode. In the proposed imaging system, the sensing mode is switched automatically by a software-controlled switch box. By obtaining a capacitive image and an inductive image after a single scan, defects in both the insulation and the conductor can be detected. In addition, comparing the two images, the location information of the defect, can also be obtained.

In this paper, the imaging mechanisms of the dual modality sensor in the capacitive mode and inductive mode are described in detail. Finite element models are presented to show the perturbation of the probing fields due to defects in the two imaging modes. An imaging system has been designed and built, and experimental results for detecting defects in insulator-metal hybrid structures are presented.

2. The Dual Modality Sensor

The coplanar dual modality sensor is a key part of the proposed imaging system and need to be designed with some care. The sensor used in this work is composed of two coplanar square spiral coils on a Printed Circuit Board (PCB), as shown in Fig. 1. The backside of the PCB is also coated as a shielding layer. The number of turns of each coil is 15, the trace width is 0.2 mm, the gap between traces is 0.2 mm, and the distance between the centres of the coil pair is 11 mm. The PCB substrate is 0.8 mm thick flame retardant woven glass reinforced epoxy resin (FR-4).

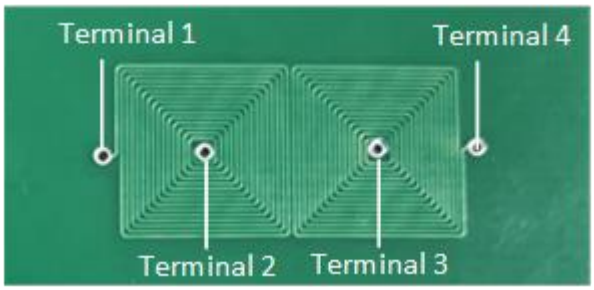

Figure 1 Dual Modality sensor layout and terminals

The PCB is held within a plastic box with four BNC connectors connecting to the four terminals of the coil pair, shown in Fig 1. The sensor can operate in two modes, namely capacitive imaging and inductive imaging. In the capacitive imaging mode, terminal 1

in Fig. 1 is connected to a driving voltage, terminal 2 and 3 are left open circuit, and terminal 4 is connected to a charge amplifier that can measure induced charge variation on the sensing coil. In the inductive imaging mode, terminal 1 is connected to the same driving voltage, terminal 2 and 3 are connected to ground, and terminal 4 is connected to a voltage amplifier that can measure the induced voltage across the sensing coil. The connection changes are implemented by a software-controlled switch box. The square electrode shape is favoured over a circular shape in this case, especially for capacitive imaging mode, as it enhances the coupling between the two coils with a smaller spacing between the two closest edges.

3. Theory

In general, an electromagnetic imaging probe used in NDE demonstrates a change of impedance as it scans over a discontinuity (*e.g.* a crack or an undesirable impurity). Auld [22, 23] has reported a reciprocity-based model of an electromagnetic probe system over a defect. Here we briefly derive the models specifically for a dual modality sensor, to provide physical insight into the influence of various parameters.

3.1 Capacitive imaging mode

In the capacitive imaging mode, one end of each planar coil is not connected, and hence the coils were effectively working as electrodes. When a sinusoidal voltage is applied to the driving electrode, a potential difference is established between the driving and sensing electrode, and thus capacitive coupling is developed. Introducing a permittivity change in the sensing area will perturb the established potential distribution and hence the capacitive coupling, the change of which can then be measured. In this mode, the driving electrode, the sensing electrode and the specimen under test can be considered as a one-port system, as shown in Fig. 2.

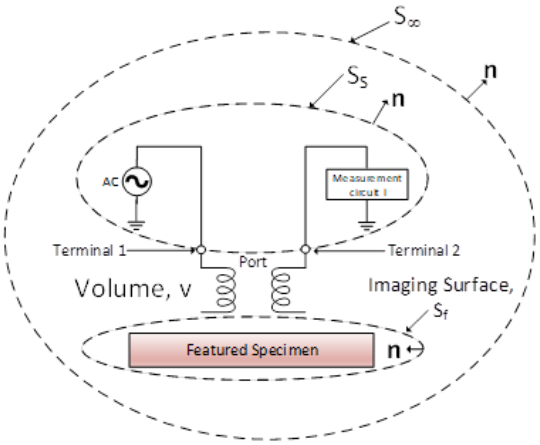

Figure 2 capacitive imaging mode geometry

The relevant form of the reciprocity relation is

$$\iint_{S_\infty + S_s + S_f} [\mathbf{E_I} \times \mathbf{H_{II}} - \mathbf{E_{II}} \times \mathbf{H_I}] \cdot \mathbf{n} ds = 0 , \tag{1}$$

where the integral is taken over the total enclosing surface of a volume without any source. S_S is the surface over the source and the measurement circuitry, S_f is the surface over the featured specimen, and $S\infty$ is the surface at the infinity. The quantities **E** and **H** are electric and magnetic fields respectively, and **n** is a unit vector normal to the surface which is directed out of the enclosed volume. The subscript I and II denote two distinct physical fields:

I. Excitation I-the "port" is excited from Terminal 1, and the specimen is in a perturbed state, i.e. the defect is presented.

II. Excitation II-the "port" is excited from Terminal 2, and the specimen is in its unperturbed state (without any defect).

The Terminal conditions for the two physical fields for the probe in capacitive mode is shown in Fig. 3.

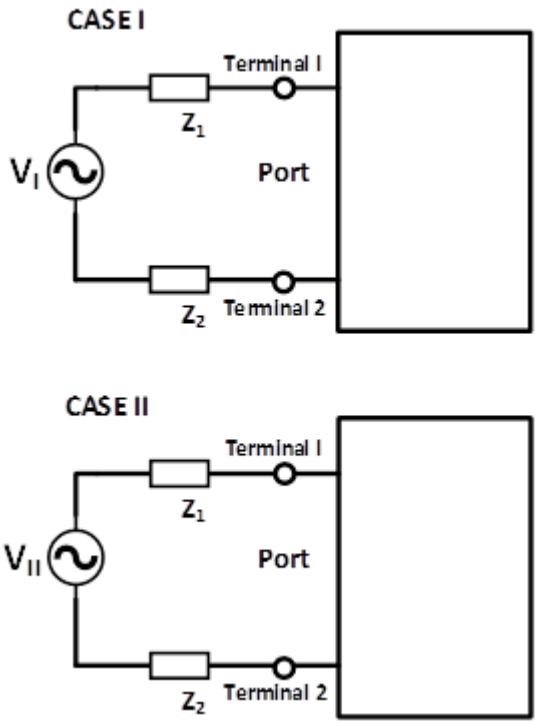

Figure 3 Terminal conditions for the two physical fields for the probe in capacitive mode ***(Is this correct? Both diagrams are the same). If this is intentional, then I would say that both cases are the same and only present one diagram.***

At infinity, the surface integral term vanishes since the wave behave as spherical waves as the radius goes to infinity and the integrand is zero on S∞. Hence, Eq. (1) reduced to

$$-\int_{S_s}\left[\mathbf{E_I}\times\mathbf{H_{II}}-\mathbf{E_{II}}\times\mathbf{H_I}\right]\cdot\mathbf{n}ds=\iint_{S_f}\left[\mathbf{E_I}\times\mathbf{H_{II}}-\mathbf{E_{II}}\times\mathbf{H_I}\right]\cdot\mathbf{n}ds \qquad (2)$$

To simplify the left hand side of Eq.(2), one should determine the field quantities on the surface Ss in terms of the drive voltage. In practice, the voltage signal is fed in to the probe via coaxial cable. The electric fields on Ss are radial ($\mathbf{E}_{Ir}$,$\mathbf{E}_{IIr}$) and the magnetic fields are circumferential ($\mathbf{H}_{I\phi}$,$\mathbf{H}_{II\phi}$). If cylindrical coordinates are used, one obtains

$$-\int_{S_s}\left[\mathbf{E_{Ir}}\mathbf{H_{II\phi}}-\mathbf{E_{IIr}}\mathbf{H_{I\phi}}\right]rdrd\phi=\iint_{S_f}\left[\mathbf{E_I}\times\mathbf{H_{II}}-\mathbf{E_{II}}\times\mathbf{H_I}\right]\cdot\mathbf{n}ds \qquad (3)$$

Using Ampere's Law, the magnetic fields can be expressed as

$$\mathbf{H_{I\phi}}=\frac{I_I}{2\pi r},\mathbf{H_{II\phi}}=\frac{I_{II}}{2\pi r}$$

Substituting into Eq.(3) one obtains

$$I_{\mathrm{I}}\int_{S_s}\mathbf{E}_{\mathbf{IIr}}dr\text{-}I_{\mathrm{II}}\int_{S_s}\mathbf{E}_{\mathbf{Ir}}dr=\iint_{S_f}\left[\mathbf{E}_{\mathbf{I}}\times\mathbf{H}_{\mathbf{II}}-\mathbf{E}_{\mathbf{II}}\times\mathbf{H}_{\mathbf{I}}\right]\cdot\mathbf{n}dS \tag{4}$$

Since

$$V_I=-\int_{S_s}\mathbf{E}_{\mathbf{Ir}}dr, V_{II}=-\int_{S_s}\mathbf{E}_{\mathbf{IIr}}dr$$

Then

$$V_{\mathrm{I}}I_{\mathrm{II}}\text{-}V_{\mathrm{II}}I_{\mathrm{I}}=\iint_{S_f}\left[\mathbf{E}_{\mathbf{I}}\times\mathbf{H}_{\mathbf{II}}-\mathbf{E}_{\mathbf{II}}\times\mathbf{H}_{\mathbf{I}}\right]\cdot\mathbf{n}dS \tag{5}$$

By substituting $V_{\mathrm{I}}Y_{\mathrm{I}}$ and $V_{\mathrm{II}}Y_{\mathrm{II}}$ for I_{I} and I_{II}, one obtains

$$\left(Y_{\mathrm{II}}\text{-}Y_{\mathrm{I}}\right)V_{\mathrm{I}}V_{\mathrm{II}}=\iint_{S_f}\left[\mathbf{E}_{\mathbf{I}}\times\mathbf{H}_{\mathbf{II}}-\mathbf{E}_{\mathbf{II}}\times\mathbf{H}_{\mathbf{I}}\right]\cdot\mathbf{n}dS \tag{6}$$

If the source is chosen such that $V_{\mathrm{II}}=V_{\mathrm{I}}$, then

$$\Delta Y=-\frac{1}{V^2}\iint_{S_f}\left[\mathbf{E}_{\mathbf{I}}\times\mathbf{H}_{\mathbf{II}}-\mathbf{E}_{\mathbf{II}}\times\mathbf{H}_{\mathbf{I}}\right]\cdot\mathbf{n}dS \tag{7}$$

Based on Gauss's Theorem, the equivalent volume representation of Eq.(7) is

$$\Delta Y=-\frac{1}{V^2}\int_{V_f}\nabla\cdot\left(\mathbf{E}_{\mathbf{I}}\times\mathbf{H}_{\mathbf{II}}-\mathbf{E}_{\mathbf{II}}\times\mathbf{H}_{\mathbf{I}}\right)dv \tag{8}$$

Where V_{f} is the volume enclosed by S_{f}. Considering vector calculus identities and using Maxwell's Equations for sinusoidal sources, one obtains

$$\Delta Y=\frac{j\omega}{V^2}\int_{V_f}\left[\left(\varepsilon_{II}-\varepsilon_I\right)\mathbf{E}_{\mathbf{I}}\cdot\mathbf{E}_{\mathbf{II}}-\left(\mu_{II}-\mu_I\right)\mathbf{H}_{\mathbf{I}}\cdot\mathbf{H}_{\mathbf{II}}\right]dv, \tag{9}$$

where ω is the frequency of the source, ε_I and μ_I are the permittivity and permeability values of the specimen (unperturbed state), ε_{II} and μ_{II} are the permittivity and permeability values of the defect in the specimen (perturbed state). The admittance (capacitance) change ΔY for the probe in capacitive mode due to the defect is then related to the electromagnetic fields presented in the region and the material characteristics.

3.2 Inductive imaging mode

In the inductive imaging mode, a voltage source between the two terminals of the driving coil cause currents flowing in the tracks of the coil and produce magnetic field, which induces voltage in the sensing coil due to magnetic induction. The conductivity and magnetic permeability of the sample affect the magnetic induction due to eddy currents and magnetic polarisation, and the effects can be measured. In this mode, the driving coil, the sensing coil and the specimen under test can be considered as a two port system, as shown in Fig.4.

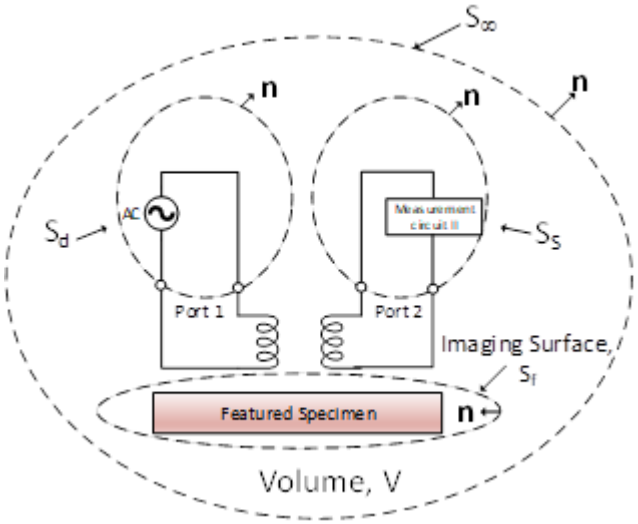

Figure 4 Inductive imaging mode geometry

The volume of interest is enclosed by surfaces labeled d, s, f and ∞ in Fig. 4. Again, two physical field excitations that are germane to the problem were considered:

I. Excitation I-the "port 1" is excited by a voltage source and the specimen is in a perturbed state, i.e. the defect is presented.

II. Excitation II-the "port 2" is excited by a voltage source and the specimen is in its unperturbed state, i.e. without any defect.

The Terminal conditions, including the Thevenin sources (V_d, V_s) and load impedances (Z_d, Z_s) for the two physical fields for the probe inductive mode is shown in Fig. 5.

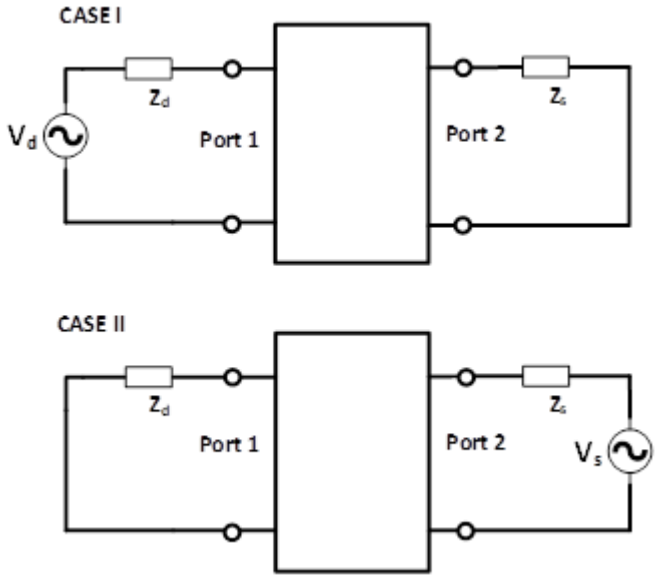

Figure 5 Terminal conditions for the two physical fields for the probe in inductive mode

The relevant form of the reciprocity relation is

$$-\int_{S_d+S_s}\left[\mathbf{E_I}\times\mathbf{H_{II}}-\mathbf{E_{II}}\times\mathbf{H_I}\right]\cdot\mathbf{n}ds=\iint_{S_f}\left[\mathbf{E_I}\times\mathbf{H_{II}}-\mathbf{E_{II}}\times\mathbf{H_I}\right]\cdot\mathbf{n}ds\,, \tag{10}$$

where S_d and S_s are two surfaces that cut across port 1 and port 2. Similar to the capacitive mode, as in Eq.(5), the integral across the probe ports (S_d and S_s) can be expressed as the products of terminal voltages and currents

$$\left(V_{1I}I_{1II}-V_{1II}I_{1I}\right)+\left(V_{2I}I_{2II}-V_{2II}I_{2I}\right)=\iint_{S_f}\left[\mathbf{E_I}\times\mathbf{H_{II}}-\mathbf{E_{II}}\times\mathbf{H_I}\right]\cdot\mathbf{n}dS \tag{11}$$

By considering the conditions at the terminals, the defect-induced change in the mutual impedance, $\Delta\mathbf{Z}$, can be obtained.

$$\Delta Z=\frac{V_{2I}}{I_d}-\frac{V_{1II}}{I_s}=-\frac{1}{I_dI_s}\iint_{S_f}\left[\mathbf{E_I}\times\mathbf{H_{II}}-\mathbf{E_{II}}\times\mathbf{H_I}\right]\cdot\mathbf{n}dS\,, \tag{12}$$

where I_d and I_s are the short circuit currents from Thevenin source "*d*" and "*s*". For a sinusoidal source, one obtains

$$\Delta Z=\frac{j\omega}{I_dI_s}\int_{V_f}\left[\left(\varepsilon_{II}-\varepsilon_I\right)\mathbf{E_I}\cdot\mathbf{E_{II}}-\left(\mu_{II}-\mu_I\right)\mathbf{H_I}\cdot\mathbf{H_{II}}\right]dv \tag{13}$$

The mutual impedance (inductance) change ΔZ for the probe in inductive mode due to the defect is also related to the electromagnetic fields presented in the region and the material characteristics.

4. Finite Element analysis

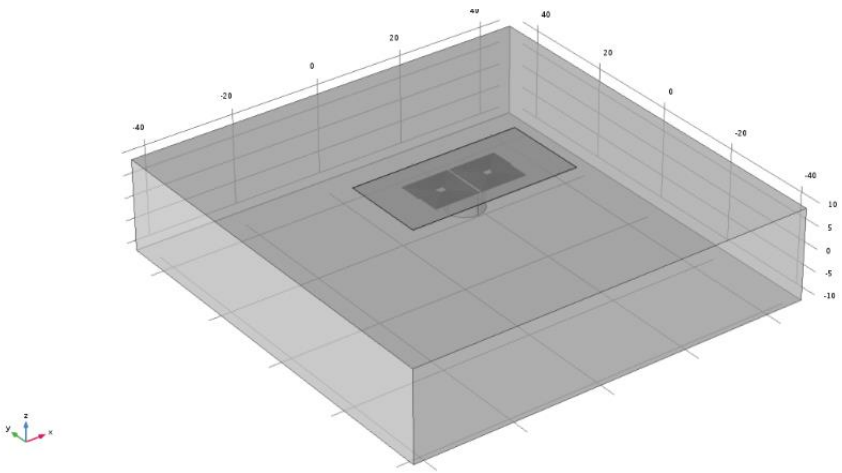

Figure 6 Geometry of FE model and its coordinate system

Finite element (FE) models were constructed in COMSOL™ to visualize the probing field perturbations due to defects in various types of materials for the capacitive and imaging modes. A 120 mm x 120 mm x 50 mm block centred at point ($x = 0$, $y = 0$, $z = 0$) was defined to be the computational domain. The size of the specimen to be tested was 90 mm x 90 mm x20 mm, and a 38 mm (x-axis) by 19 mm (y-axis) rectangular area was drawn on the $z = 10.5$mm plane and extruded upwards (positive z direction) to form the 0.8 mm thick plate representing the dielectric substrate of the sensor, as shown in Fig. 6. The sensor surface was centred at ($x = 0$, $y = 0$, $z = 10.5$). The sensor geometry in the FE models was the same as the probe shown in Fig. 1. The material of the insulating substrate of the PCB was set to be FR-4, and accordingly, the dielectric constant was set to 4.5. Since the coils/electrodes and backplane are very thin copper layers (60 μm), they were treated as boundaries rather than sub-domains. This can reduce the computation complexity greatly, as very thin sub-domains will require very fine mesh elements and will increase the total number of the elements required.

For the capacitive imaging mode, the coils worked as electrodes, with the excitation frequency being 10 kHz or even lower so that the effects of electric field were maximized. Therefore, an electrostatic analysis should be adequate to describe the capacitive imaging mode and a DC excitation on the driving electrode was used in the FE models. The first set of models are with plastic specimens 0.5 mm off the sensor surface (dielectric constant was set to 4). The electric field distributions in the x=0 plane,

y=0 plane and z=10 plane (the surface of the specimen) from the planar sensor for a sound specimen and a specimen with a flat-bottomed hole (8 mm in diameter and 5 mm deep) are plotted in Figure 7.

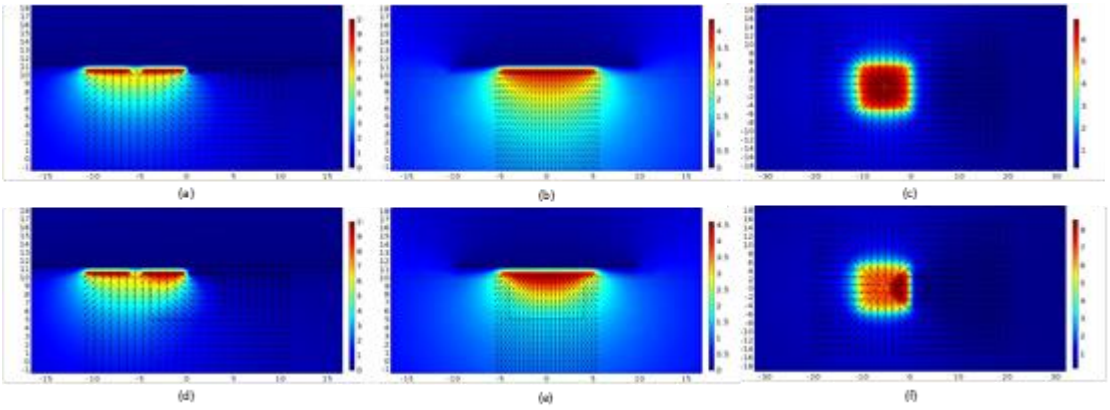

Figure 7 Electric field and electric potential for a sound plastic specimen (a) x=0 plane, (b)y=0 plane, (c) z=10plane; Electric field and electric potential for a specimen with a flat-bottomed hole (d) x=0 plane, (e)y=0 plane, (f)z=10 plane;

It can be seen from Fig 7 that the electric potential distribution and the electric field lines are all altered due to the presence of the defect.

The second set of models were with metal specimens (electrically grounded aluminium specimens) 0.5 mm off the sensor surface. The electric field distributions in the x=0 plane, y=0 plane and z=10 plane (the surface of the specimen) from the planar sensor for a sound specimen and a specimen with a flat-bottomed hole (8 mm in diameter and 5 mm deep) are plotted in Fig. 8. It can be seen from Fig 8 that the electric field lines terminated on the conducting surface, so that the open hole greatly affected the field lines, leading to a significant change in the electric field distribution.

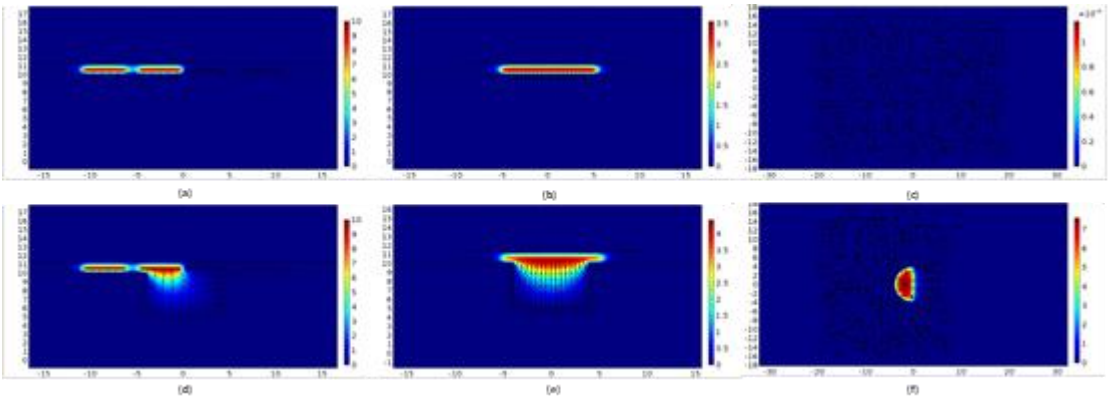

Figure 8 Electric field and electric potential for an undamaged aluminium specimen (a) x=0 plane, (b) y=0 plane, (c) z=10 plane; Electric field and electric potential for

a specimen with a flat-bottomed hole for (d) x=0 plane, (e) y=0 plane,and (f) z=10 plane;

For the inductive imaging mode, the coils in the FE models were directly defined as multi-turn coils in the plane instead of drawing the actual geometry, a simplification that reduced the computation cost.

The third set of models were with metal specimens 0.5 mm off the sensor surface (electrically grounded aluminium specimens). The magnetic field and the induced eddy current in the x=0 plane, y=0 plane and z=10 plane (the surface of the specimen) from the planar sensor for a sound specimen and a specimen with a crack (10 mm in diameter and 5 mm deep) are plotted in Fig.9. Figs. 9(a) to Fig. 9 (c) show the magnetic fields and the eddy currents for a sound specimen. Fig 9(d) to Fig. 9 (f) show the magnetic fields and the eddy currents for a specimen with a crack, and the crack is parallel with the line of coil centres (referred to as “parallel” case hereafter). Fig 9(g) to Fig. 9 (i) show the magnetic fields and the eddy currents for a specimen with a crack, and the crack is perpendicular to the line of coil centres (referred to as “perpendicular” case hereafter). Comparing Fig.9 (a) to (i), the presence of the crack will perturb the magnetic field and induced eddy current. It can also be seen that the perturbation is more significant in the “parallel” case. This indicate that in the inductive imaging mode, the imaging performance is direction sensitive and the “parallel” case will provide the best result, and will be used in the remaining part of this work.

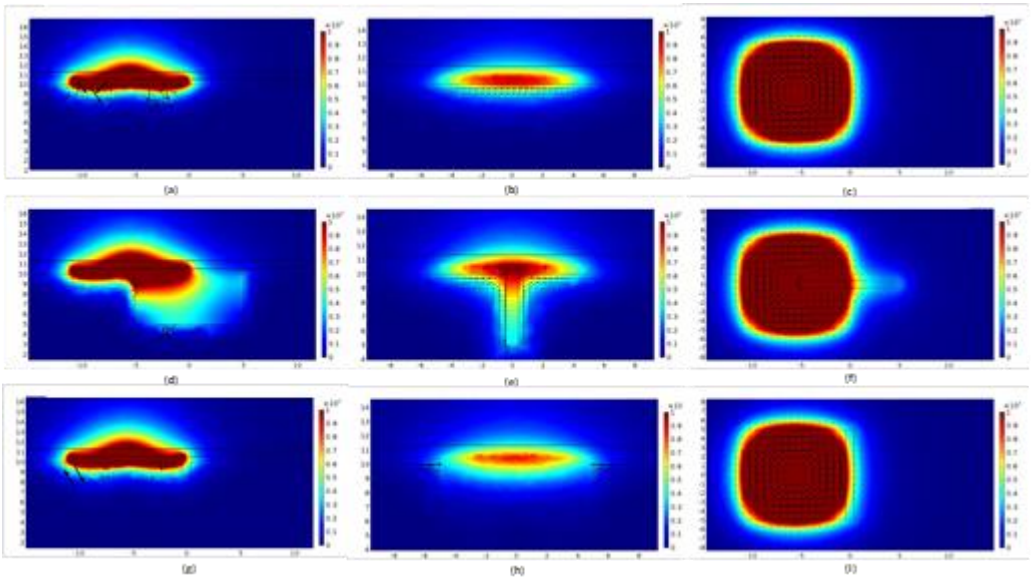

Figure 9. Top row Magnetic field and eddy current for an undamaged polymer sample (a) x=0 plane, (b) y=0 plane, (c) z=10 plane. Middle row: Magnetic field and eddy

current for a specimen with a crack ("parallel" case) (d) x=0 plane, (e) y=0 plane, (f) z=10 plane. Bottom row: Magnetic field and eddy current a specimen with a crack ("perpendicular" case) (g) x=0 plane, (h) y=0 plane, (i) z=10 plane;

The ability of the proposed coplanar sensor for defect detection in the insulator/conductor hybrid structure can also be demonstrated with an FE model. In this FE model, a 2 mm thick plastic board with three holes was placed on top of a 20 mm thick aluminium plate with four surface holes, as shown in Fig. 10. The dimensions of the holes are shown in Table 1.

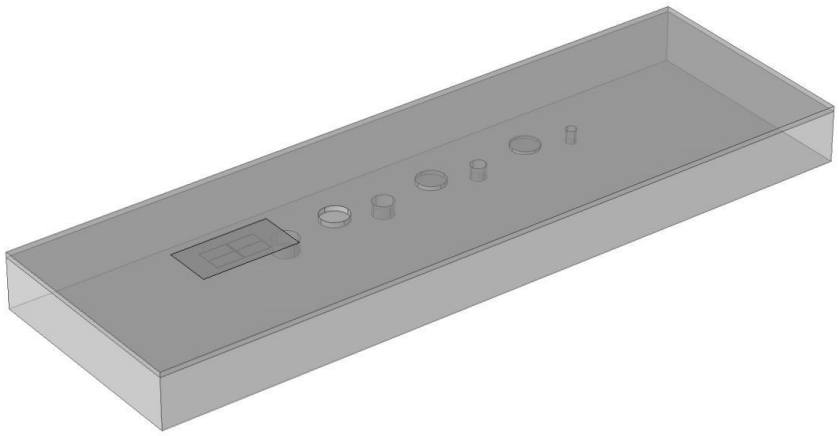

Figure 10 FE model geometry for a hybrid specimen

Table 1. Dimensions of the FE model shown in Fig. 10.

No.	Location	Height	Diameter	Remaining Thickness from top (mm)
1	Polymer plate	2.0	10.0	0
2	Polymer plate	1.5	10.0	0.5
3	Polymer plate	1.0	10.0	1.0
4	Aluminium plate	5.0	10.0	2.0
5	Aluminium plate	5.0	8.0	2.0
6	Aluminium plate	5.0	6.0	2.0
7	Aluminium plate	5.0	4.0	2.0

A simulated line scan was performed across the defects along the central line. The FE model was defined and solved for both the capacitive and inductive modes respectively. In the capacitive imaging mode, the amount of induced charges on the sensing electrode was calculated, as shown in Fig 11(a). In the inductive mode, the induced voltage across the sensing coil is calculated, as shown in Fig 11(b). The data are displayed as Variation Ratios (*VR*) throughout this work for consistency and direct comparison. The *VR* is calculated using Eq.(14)

$$VR = (V_m - V_0) / V_0 , \tag{15}$$

where V_m is the value at each scan position, and V_0 is the background value when there is no defect.

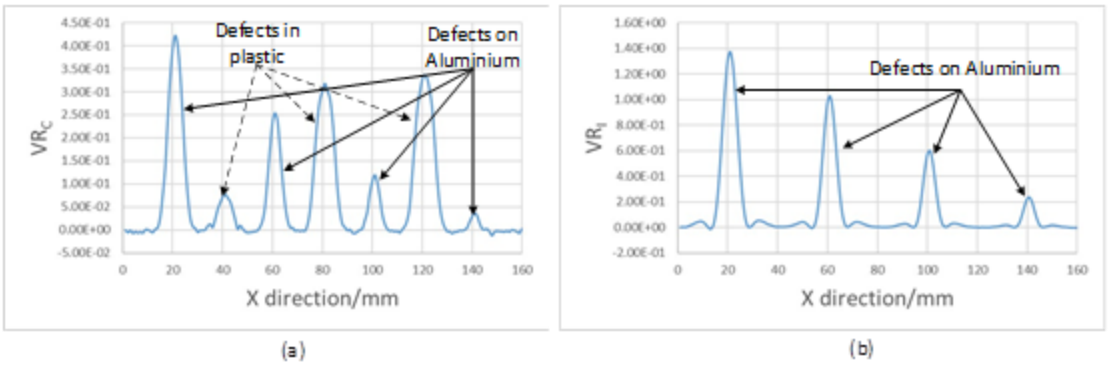

Figure 11 Simulated line scans (a) capacitive imaging mode and (b) inductive imaging mode;

It can be seen from Fig. 11 that the sensor is sensitive to defects in the plastic board and on the aluminium surface in the capacitive imaging mode. In the conductive imaging mode, the sensor is only sensitive to surface features on aluminium. In both plots, the *VR*s for the four holes on the aluminium can reflect the relative depths of the holes. The *VR*s for the holes in plastic board does not show such a trend because the negative measurement sensitivity values will affect the sensor response due to hidden defect in non-conducting specimen [24]. From Figs. 11(a) and (b), one could discriminate the location the defects in the non-conductor/ conductor hybrid structure.

5. Experimental setup and results

To use the above dual modality imaging concepts to practice, it is necessary to consider the associated electronic switching and measuring circuitry. The sensor shown in Fig. 1 has four terminals connected to the ends of the driving and sensing coil pair. A 10 kHz 10V pk-pk diving voltage (unless stated otherwise) from a signal generator (Tektronix^{TM} AFG1022) is fed into the sensor via Terminal 1. Terminal 2 and 3 are connected to ground through two SPST switches (Analog Device^{TM} ADG902). The sensing signal is taken from Terminal 4 and a SPDT switch (Analog Device^{TM} ADG919) is used as a 2:1 de-multiplex to switch the signal between a charge amplifier (in the capacitive mode) and a voltage amplifier (in the inductive mode). Another SPDT switch (Analog Device^{TM} ADG919) is then used to multiplex the pre-amplified signals to a

lock-in amplifier (Signal Recovery™ 7230). The DC output from the lock-in amplifier is acquired by the DAQ card in the NI PXI system.

To perform an X-Y scan over a specimen, the sensor is held and manipulated by an X-Y scanning stage. At each scanning position, the switches change their states once, and the readings from the capacitive imaging mode and inductive imaging mode are obtained and stored separately. The switches, the scanning stage and the data acquisition system are all controlled by software developed in LabVIEW and installed in the NI PXI system. Two images, namely capacitive image and inductive image, can be formed after a completed step-by-step scan.

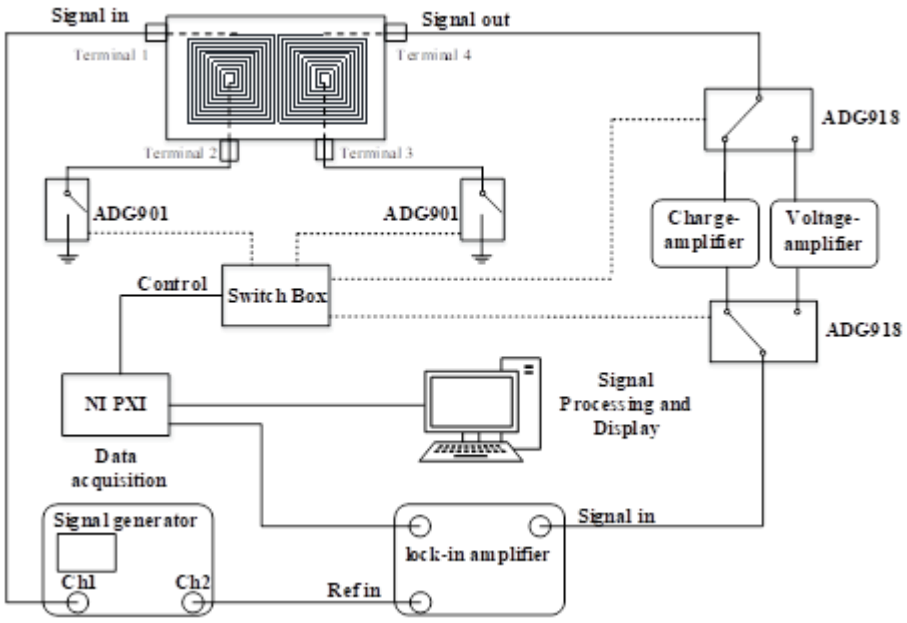

Figure 12 Experimental setup

The first specimen inspected in this paper is an aluminium-glass fibre composite board hybrid structure (referred to as Specimen 1). The 280 mm by 90 mm aluminium plate is with four 5 mm deep flat-bottomed circular holes. The diameters of the holes are 10 mm, 8 mm, 6 mm and 4 mm. A 2 mm thick glass fibre composite board with three holes of the same diameter (11 mm) and different depths (2 mm, 1.5 mm and 1 mm) was placed on top of the aluminium board, and the three shallower holes are hidden if seen from the top, as shown in Fig. 13.

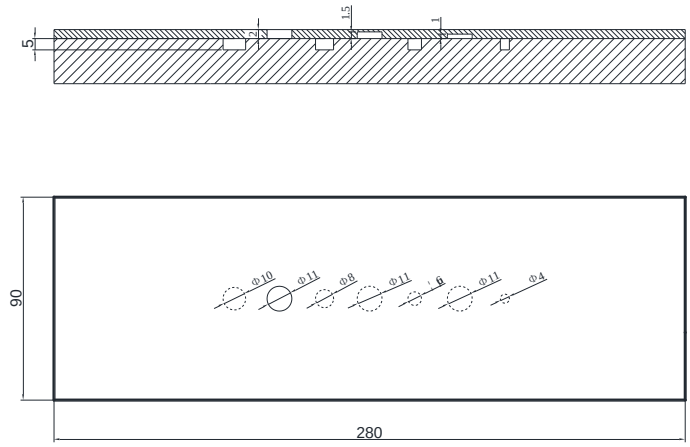

Figure 13 Geometry of Specimen 1

The probe shown in Fig. 1 was scanned over a 30 mm by 140 mm area at a 0.5 mm lift-off. Capacitive image and inductive images were obtained after a single scan, as shown in Fig. 14.

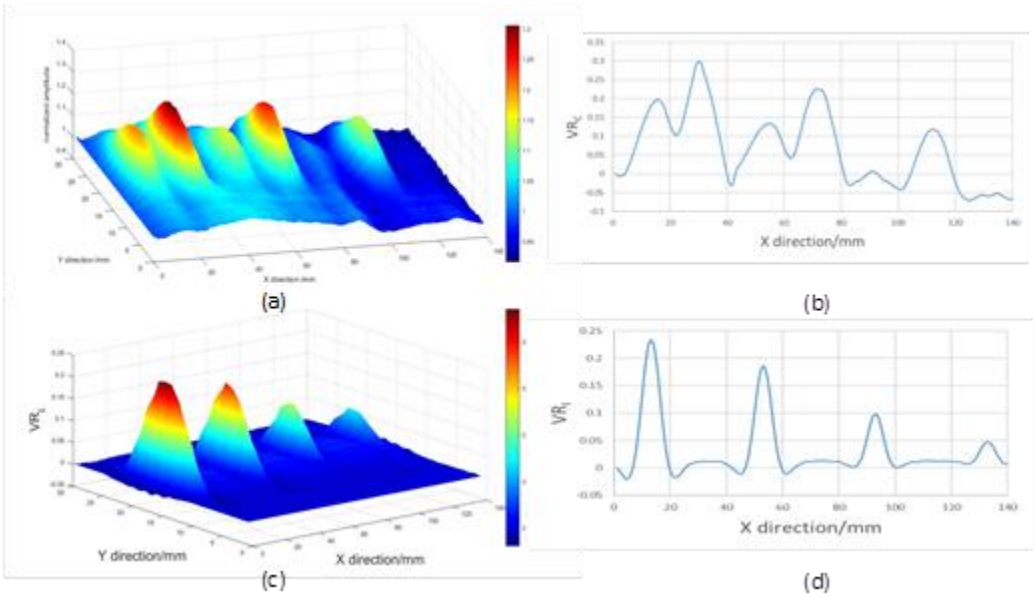

Figure 14 Experimental results for Specimen 1: (a) capacitive image, (b) line scan plot from capacitive mode,(c) inductive image and (d) line scan plot from inductive mode

As in the FE models, the experimental data are also displayed as variation ratios (*VR*) throughout this work for consistency and direct comparison. For a clearer display, the data on the central line along the features were extracted and plotted separately, as shown in Fig. 14(b). It can be seen from the capacitive image (Fig.14(a)) all the holes,

both in the aluminium and glass-fibre plates, were detected. This is due to the fact that the probing field is sensitive to features in both non-conducting materials and on the conducting surface in the capacitive imaging mode. In the inductive image, only the four holes on the aluminium board surface were detected, but the size of each hole can be inferred from the indications in the image. It can be seen from Fig. 14 that the indications for the four holes are of decreasing amplitude for smaller hole diameters.

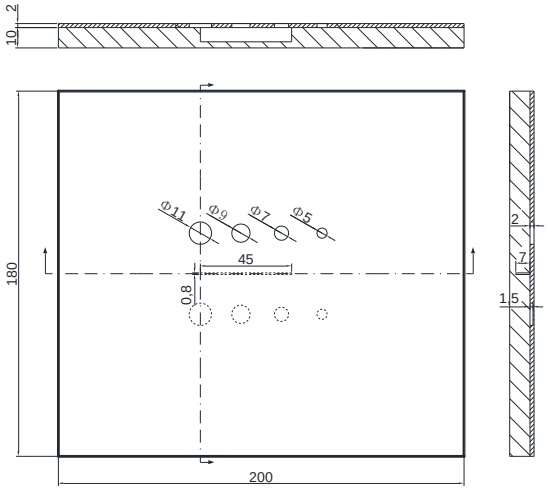

Figure 15 Geometry of Specimen 2

The second specimen was also an aluminium-glass fibre composite hybrid structure (Specimen 2). The aluminium plate contained a 46 mm (length) by 7 mm (depth) by 0.8 mm (width) crack. The glass fibre composite contained two sets of holes. One set of holes were through-holes with diameters of 11 mm, 9 mm, 7mm and 5mm, and the others were 1.5 mm deep flat-bottomed holes with diameters of 11 mm, 9 mm, 7mm and 5mm. The probe shown in Fig. 1 was scanned over a 90 mm by 100 mm area at a 0.5 mm lift-off.

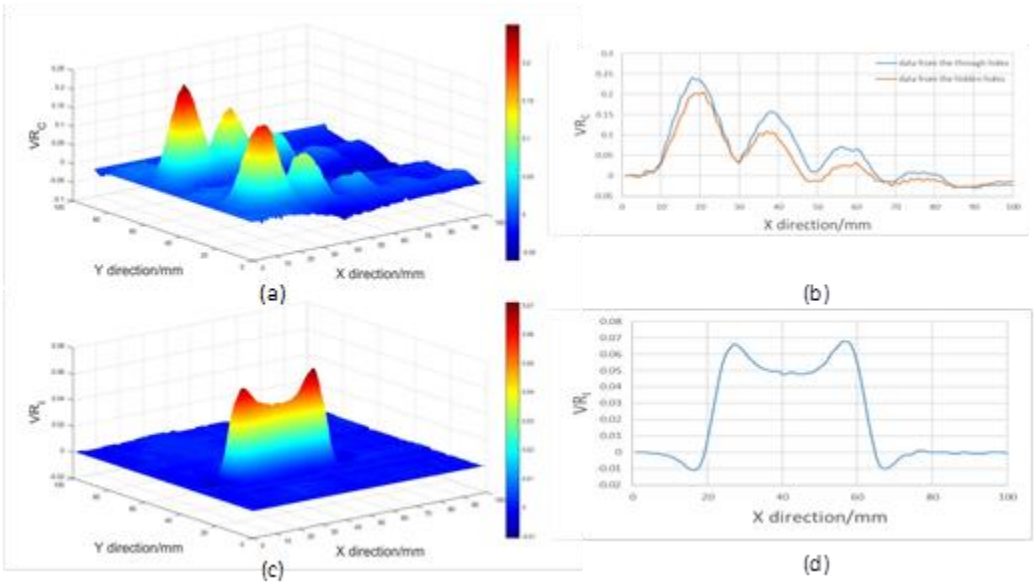

Figure 16 Experimental results for Specimen 2: (a) capacitive image, (b) line scan plot from capacitive mode, (c) inductive image and (d) line scan plot from inductive mode.

The capacitive image and inductive image were obtained after a single scan, as shown in Fig. 16. Both the through holes and hidden hole in the glass fibre composite board were appeared as indications in the capacitive image, but the crack could not be seen in the capacitive image, due to its small opening. In the inductive image, the crack is clearly seen, but the features in the glass fibre composite board are absent.

Further experiments were also carried out to explore the ability of the proposed system in imaging hidden defects in metal and thin cracks. A third scan was thus performed with the aluminium board (Specimen 3) shown in Fig. 17.

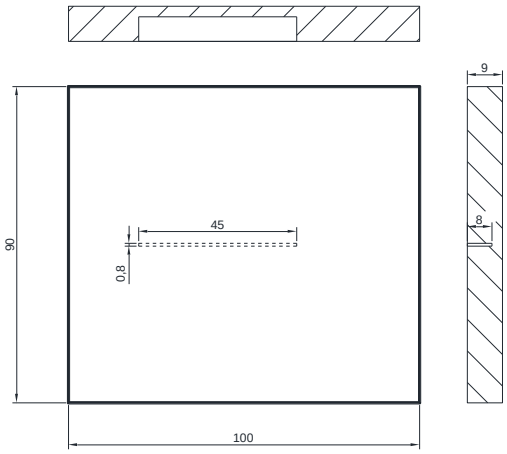

Figure 17 Geometry of Specimen 3

To achieve a bigger penetration, a reduced excitation frequency was used. The probe was excited by a 2 kHz 10V pk-pk voltage and the scan was taken from the sound face, in which case, the crack is hidden from the top surface. The hidden crack formed a clear indication in the inductive image as shown in Fig. 18. The signal to noise ratio was low compared to the previous experiments, as the hidden crack caused only a slight perturbation of the eddy current and magnetic field. The capacitive image is not included as the capacitive coupling is insensitive to features under a conducting surface.

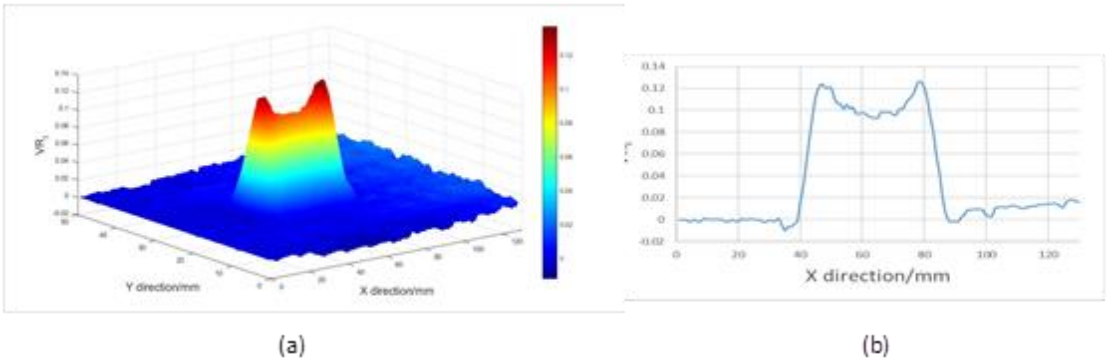

Figure 18 Experimental results for Specimen 3: (a) inductive image and (b) line scan plot from inductive mode

A fourth scan was performed on a carbon steel specimen with three narrow cracks (Specimen 4). The geometries of the cracks are shown in Fig. 19. with the dimensions indicated in Table 2.

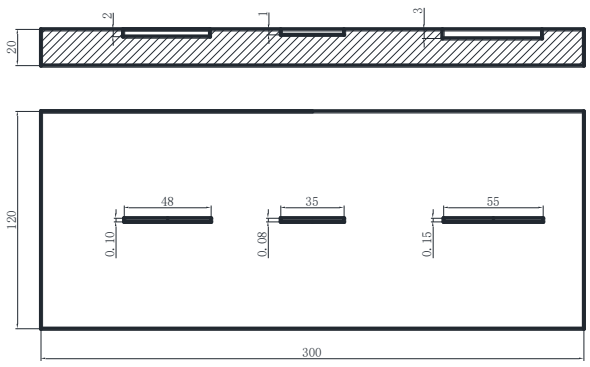

Figure 19 Geometry of Specimen 4

Table 2 Dimensions of the cracks in the carbon steel specimen

	Length (mm)	Width (mm)	Depth (mm)
Crack 1	48.00	0.10	2.00
Crack 2	35.00	0.08	1.00
Crack 3	55.00	0.15	3.00

A line scan was performed along the three cracks and the data from the inductive imaging mode was plotted in Fig.20. It can be seen that all the three cracks are detected.

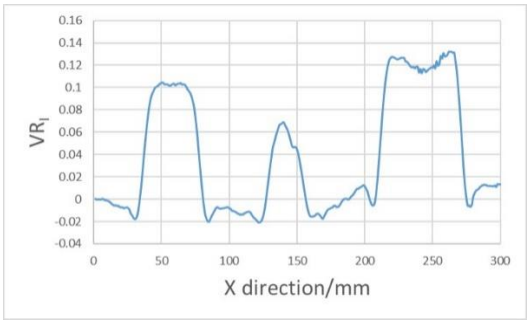

Figure 20 Experimental results for Specimen 4

6. Discussion and Conclusions

In this work, a dual modality electromagnetic imaging system is presented. In such a system, the coplanar sensor acts as a spiral coil pair, or as a planar electrode pair depending on the imaging mode. The formulas developed in Section 3 give explicit mathematical expressions for the changes in impedance (admittance in capacitive mode and mutual inductance in inductive mode) of the sensor in terms of electric and magnetic field distribution of the sensor with varying material properties of the specimen under test. The FE models of the dual modality sensor are set up to analyse the field perturbation around various defects in the specimen under test for both modes. Experiments were carried out to demonstrate the ability of this proposed system to detect and distinguish defects in the glass fibre composite board-aluminium hybrid structure. In the capacitive imaging mode, the imaging system can be used to investigate the properties and structures of both conductive and dielectric materials. For conductors, only surface feature can be extracted, as charges accumulated on the surface blind the probe to interior features. For dielectric materials, both surface and interior features can be examined. In the inductive imaging mode, the system can be used to interrogate specimens that are conductive, and can analyse sub-surface features of these specimen, provided the features lie within the skin depth of the specimen. The versatility of the

system is also demonstrated with a scan on a carbon steel specimen with three narrow cracks.

The experimental results suggest that the proposed system has the potential to inspect insulators, conductors and composite materials/structures. In addition, comparison between the capacitive image and inductive image can provide information for defect location discrimination. The co-planar nature of the sensor makes it readily to be fabricated with flexible materials for uneven surface inspection. Future research will focus on optimisation of sensor geometries for specific measurement applications such as the non-destructive evaluation of composite materials and curved structures.

Acknowledgements

This work was funded by the National Natural Science Foundation of China (No. 51675536 and No. 51574276), and the Fundamental Research Funds for the Central Universities (No.18CX02084A).

[1] J. Jiao, L. Li, B. Wu, and C. He, "Novel capacitive proximity sensors for assessing the aging of composite insulators," *Sensors and Actuators A: Physical,* vol. 253, pp. 75-84, 2017/01/01/ 2017.

[2] T. Chen and N. Bowler, "Design of interdigital spiral and concentric capacitive sensors for materials evaluation," *AIP Conference Proceedings,* vol. 1511, no. 1, pp. 1593-1600, 2013/01/25 2013.

[3] X. Yin and D. A. Hutchins, "Non-destructive evaluation of composite materials using a capacitive imaging technique," *Composites Part B-Engineering,* vol. 43, no. 3, pp. 1282-1292, APR 2012 2012.

[4] A. A. Nassr, W. H. Ahmed, and W. W. El-Dakhakhni, "Coplanar capacitance sensors for detecting water intrusion in composite structures," *Measurement Science and Technology,* vol. 19, no. 7, p. 075702, 2008.

[5] M. Morozov, W. Jackson, and S. G. Pierce, "Capacitive imaging of impact damage in composite material," *Composites Part B: Engineering,* vol. 113, pp. 65-71, 2017/03/15/ 2017.

[6] X. Yin, D. A. Hutchins, G. G. Diamond, and P. Purnell, "Non-destructive evaluation of concrete using a capacitive imaging technique: Preliminary modelling and experiments," *Cement and Concrete Research,* vol. 40, no. 12, pp. 1734-1743, DEC 2010 2010.

[7] Y. Cheng, F. Gao, A. Hanif, Z. Lu, and Z. Li, "Development of a capacitive sensor for concrete structure health monitoring," *Construction and Building Materials,* vol. 149, pp. 659-668, 2017/09/15/ 2017.

[8] T. Chen and N. Bowler, "A capacitive probe for quantitative nondestructive evaluation of wiring insulation," *NDT & E International,* vol. 52, no. 0, pp. 9-15, 2012.

[9] X. a. Yuan *et al.*, "Inspection of both inner and outer cracks in aluminum tubes using double frequency circumferential current field testing method," *Mechanical Systems and Signal Processing,* vol. 127, pp. 16-34, 2019/07/15/ 2019.

[10] X. Yuan, W. Li, G. Chen, X. Yin, W. Yang, and J. Ge, "Two-Step Interpolation Algorithm for Measurement of Longitudinal Cracks on Pipe Strings Using Circumferential Current Field Testing System," *IEEE Transactions on Industrial Informatics,* vol. 14, no. 2, pp. 394-402, 2018.

[11] Z. Deng, Y. Kang, J. Zhang, and K. Song, "Multi-source effect in magnetizing-based eddy current testing sensor for surface crack in ferromagnetic materials," *Sensors and Actuators A: Physical,* vol. 271, pp. 24-36, 2018/03/01/ 2018.

[12] L. Barbato, N. Poulakis, A. Tamburrino, T. Theodoulidis, and S. Ventre, "Solution and Extension of a New Benchmark Problem for Eddy-Current Nondestructive Testing," *IEEE Transactions on Magnetics,* vol. 51, no. 7, pp. 1-7, 2015.

[13] D. Wen, M. Fan, B. Cao, and B. Ye, "Adjusting LOI for Enhancement of Pulsed Eddy Current Thickness Measurement," *IEEE Transactions on Instrumentation and Measurement,* pp. 1-7, 2019.

[14] J. Zhu, G. Tian, Q. Min, and J. Wu, "Comparison Study of Different Features for Pocket Length Quantification of Angular Defects Using Eddy Current Pulsed Thermography," *IEEE Transactions on Instrumentation and Measurement,* vol. 68, no. 5, pp. 1373-1381, 2019.

[15] K. Mizukami, Y. Mizutani, A. Todoroki, and Y. Suzuki, "Detection of in-plane and out-of-plane fiber waviness in unidirectional carbon fiber reinforced composites using eddy current testing," *Composites Part B: Engineering,* vol. 86, pp. 84-94, 2016/02/01/ 2016.

[16] W. Cheng, "Pulsed Eddy Current Testing of Carbon Steel Pipes' Wall-thinning Through Insulation and Cladding," *Journal of Nondestructive Evaluation,* vol. 31, no. 3, pp. 215-224, 2012/09/01 2012.

[17] C. S. Angani, D. G. Park, G. D. Kim, C. G. Kim, and Y. M. Cheong, "Differential pulsed eddy current sensor for the detection of wall thinning in an insulated stainless steel pipe," *Journal of Applied Physics,* vol. 107, no. 9, p. 09E720, 2010/05/01 2010.

[18] B. George, H. Zangl, T. Bretterklieber, and G. Brasseur, "A Combined Inductive–Capacitive Proximity Sensor for Seat Occupancy Detection," *IEEE Transactions on Instrumentation and Measurement,* vol. 59, no. 5, pp. 1463-1470, 2010.

[19] J. Long and B. Wang, "A metamaterial-inspired sensor for combined inductive-capacitive detection," *Applied Physics Letters,* vol. 106, no. 7, p. 074104, 2015/02/16 2015.

[20] S. Gäbler, H. Heuer, and G. Heinrich, "Measuring and Imaging Permittivity of Insulators Using High-Frequency Eddy-Current Devices," *IEEE Transactions on Instrumentation and Measurement,* vol. 64, no. 8, pp. 2227-2238, 2015.

[21] J. R. S. Avila, K. Y. How, and W. Yin, "A novel dual modality sensor with sensitivities to permittivity and conductivity," in *2017 IEEE International Instrumentation and Measurement Technology Conference (I2MTC)*, 2017, pp. 1-6.

[22] B. A. Auld, A. V. Clark, S.R.Schaps, and P.R.Heyliger, "capacitive probe array measurement and limitations," in *Review of Progress in Quantitative Nondestructive Evaluation*, 1993, pp. 1063-1070.

[23] A. J. Bahr and B. A. Auld, "An electromagnetic model for eddy-current imaging," *Journal of Nondestructive Evaluation,* vol. 7, no. 1, pp. 71-77, 1988/06/01 1988.

[24] X. Yin, C. Li, Z. Li, W. Li, and G. Chen, "Lift-off Effect for Capacitive Imaging Sensors," *Sensors,* vol. 18, no. 12, 2018.